

# Temperature-Independent Coercivity in Compositionally Graded Ferromagnetic Multilayers

M. Quintana<sup>1,\*</sup>, A. Meléndez<sup>1,2</sup>, C. Martín Valderrama<sup>1</sup>, L. Fallarino<sup>1,3</sup> and A. Berger<sup>1</sup>

<sup>1</sup>*CIC nanoGUNE BRTA, Tolosa Hiribidea 76, E-20018 Donostia, San Sebastián, Spain*

<sup>2</sup>*University of the Basque Country UPV/EHU, E-48080 Bilbao, Spain*

<sup>3</sup>*CIC energiGUNE BRTA, Álava Technology Park, C/Albert Einstein 48, Miñano 01510, Spain*

(Received 20 April 2022; revised 1 August 2022; accepted 29 September 2022; published 9 November 2022)

We devise nanoscale-designed ferromagnetic thin films with graded exchange-coupling ( $J$ ) profiles that allow us to obtain constant coercivities over a very extended temperature range. The magnetic structure designed here is composed of two ferromagnetic layers, which are separated by a spacer layer with a linear exchange-graded profile. Our detailed magnetometry analysis on single-crystal Co-Ru alloy thin films reveals a coercivity plateau with a relative change of less than 2% over a temperature range of 75 K, whereas conventional films exhibit changes larger than 20%. This remarkable behavior is achieved by means of a strongly temperature-dependent exchange bias between adjacent ferromagnetic portions of our film structures, which are designed to fully compensate for the conventional temperature dependence of the coercive field. This strongly temperature-dependent bias field is mediated by a paramagnetic interlayer in our film design and can be adjusted by a suitable choice of both the spacer-layer composition profile and thickness. Our particular design can be applied to a large variety of magnetic materials and adapted to relevant temperature ranges that are needed to maintain stable coercive field values over a wide operation range in real applications.

DOI: 10.1103/PhysRevApplied.18.054024

## I. INTRODUCTION

The design of ferromagnetic materials with unique magnetic properties is of central relevance, in both the context of fundamental science and regarding applications in industry [1–3]. In particular, magnetization-reversal behavior, its detailed understanding, and its design modifications have been key areas of research during the last decades [4,5]. Fundamentally, magnetization reversal describes a change in the direction of magnetization vector,  $M$ , and it is most commonly achieved by the application of an external magnetic field,  $H$ . This process is associated with a first-order phase transition triggered by the inversion of the magnetic field direction at temperatures,  $T$ , below the Curie temperature,  $T_C$  [6]. Due to the nature of first-order phase transitions, the reversal described by the  $M(H)$  curve is typically hysteretic, and its width is characterized by the coercive field,  $H_c$ , which, in turn, is a core quantity to describe the magnetic properties of materials. Hereby, the manipulation of  $H_c$  by means of material selection and design is a crucial field of research because small  $H_c$  values (i.e., soft ferromagnetic materials) are required for magnetocaloric [7–10] and energy-conversion [11,12] applications, while larger  $H_c$  (semihard and hard ferromagnets) are more commonly used for data storage

[13–16] or green technology components, such as electric motors [17,18].

Many of these applications, such as the write cycle in data storage, rely on very specific magnetization switching points, and thus, reliable  $H_c$  values and associated narrow distributions are required to achieve a stable operation point. This phenomenon is particularly relevant in magnetic-tunnel-junction- (MTJ) based data-storage technologies [19,20]. For example, in spin-orbit torque (SOT) and spin-transfer-torque (STT) magnetic random-access memories (MRAM), relatively high current densities have to be applied to switch the magnetic free layer [21–23]. This, in turn, can lead to relevant self-heating effects, including in devices of ever-decreasing size [24–27], which can subsequently lead to substantial modifications of the device's ferromagnetic properties, in particular, its magnetization-reversal threshold. Moreover, these self-heating effects are demonstrated to cause difficulties in keeping operation points stable, and thus, overall device reliability [28,29]. Furthermore, dependable device operation requires the utilization of overdrive margins to ensure the switching of devices over the entire certified temperature range of operation, which conventionally requires a substantial extra overdrive margin due to temperature-dependent switching and coercive fields [30].

\*m.quintana@nanogune.eu

In general, coercivity in ferromagnets is a strongly temperature-dependent quantity because it relies on thermal activation processes that trigger the first-order phase transition of magnetization reversal. In this context, many approaches are considered to suppress, or at least reduce, the  $H_c$  versus  $T$  dependence for applications that require specific target values for operations, such as microstructure modifications via material substitutions [31–33] or exchange-spring-media designs of multilayer systems [34–38]. Still, most of these material designs rely on very specific material choices that constrain their broad-based applicability. Furthermore, achieving an actual plateau of constant  $H_c$  in a specifically selected  $T$  range is extremely difficult following any of these approaches. Thus, there is still a very clear need for specifically functionalized material designs, in which the temperature dependence of coercivity can be limited or, in general, controlled at will over a predefined temperature range and with very flexible material choices. Here, we present a multilayer structure for exactly this purpose that is fundamentally compatible with layer sequences used in devices, with which we can reduce or even suppress the  $H_c$  versus  $T$  dependence of a ferromagnetic (FM) film over an extended  $T$  range. Accordingly, our multilayers might prove to be extremely useful for MRAM technology and, more generally, magnetic data storage and processing devices that rely on stable operation points under variable application conditions.

As a starting point, we consider the fact that thin films with compositionally graded profiles have arisen as a powerful material design to tune magnetic states and their magnetization reversal overall [39–41]. Hereby, recent studies have demonstrated that such compositional gradients can be utilized to fabricate film structures, in which the exchange energy is depth dependent [42–44]. This approach has even demonstrated the ability to suppress coercivity in anisotropic materials over significant temperature ranges [45], which might be especially relevant in the context of magneto-caloric applications [46]. Therefore, these materials with exchange-graded profiles (EGPs) should have the potential to control the temperature dependence of coercivity upon using a suitable choice of material profiles.

One of the key aspects of such EGPs from a thermodynamics perspective is that their resulting temperature dependent magnetization profiles can exhibit spatial variations down to the 1–2 nm length scale [43]. This means that, despite the fact that ferromagnetism is a long-range collective phenomenon at  $T < T_C$ , an exchange-graded ferromagnet will behave at each depth as if its magnetic properties were predominantly controlled by a “local” Curie temperature,  $T_C^{\text{loc}}$ , that is only proportional to the local effective exchange energy. This remarkable phenomenon can be extremely useful to accurately tune and control magnetization profiles as a function of temperature [44,46] and, correspondingly, it can be used to design films

that exhibit exchange-coupling everywhere, but form separate FM and quasiparamagnetic (PM) layered portions for specific temperature ranges [44,47–49].

Here, we successfully show the viability of this approach to construct materials that exhibit constant  $H_c$  values over extended temperature ranges upon utilizing a proper EGP material design. In Sec. II of this work, we present core structural and magnetic properties of our EGP-containing films and discuss key aspects of our sample fabrication. In Sec. III, we present magnetometry data that demonstrate the viability of our approach and exhibit very wide  $H_c$  versus  $T$  plateau regions. In Sec. IV, we present a model that aids a quantitative understanding of this magnetization-reversal behavior. In the last section, we draw some general conclusions and provide an outlook based on the accomplishments presented here.

## II. MATERIAL DESIGN

Following the aforementioned strategy, we design magnetic films containing EGPs of the type schematically shown in Fig. 1. Here, we display the  $T_C^{\text{loc}}$  profile as a function of film depth  $z$ . Our profile is composed of three different segments. First, a base FM layer that has a large and constant ordering temperature,  $T_C^{\text{loc}} = T_C^B$ . The second layer consists of an EGP structure of thickness  $t$ , the  $T_C^{\text{loc}}$  of which decreases linearly from  $T_C^B$  to  $T_C^G < T_C^B$ . Finally,

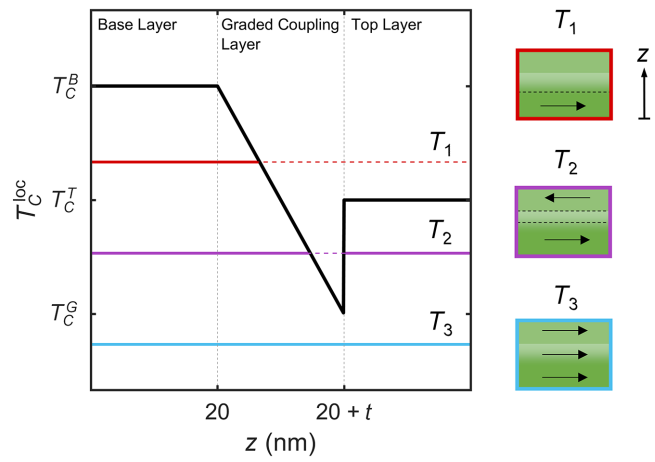


FIG. 1. Schematic of  $T_C^{\text{loc}}$  as a function of depth  $z$  in a multilayer sequence composed of a base layer with high  $T_C^B$ , a top layer with intermediate  $T_C^T$ , and an intermediate layer with an exchange-graded profile. Solid portions of the horizontal colored lines represent the regions of the film, in which a FM state can be expected for three different temperatures  $T_1$ ,  $T_2$ , and  $T_3$ , while the dashed lines symbolize presumed PM regions. On the right-hand side of the main figure, schematics of the FM magnetization profiles are displayed for the three highlighted temperatures. Green color grading represents the local exchange energy, and black-dashed lines represent the expected PM/FM interfaces. Arrows represent the portion of the film exhibiting a FM state.

the structure has a top layer with a constant  $T_C^{\text{loc}} = T_C^T$ , such that  $T_C^G < T_C^T < T_C^B$ . Within the local Curie temperature picture, we now expect, for temperatures  $T_1$  with  $T_C^T < T_1 < T_C^B$ , symbolized in red in Fig. 1, that only the base FM and part of the graded structure will be in its ferromagnetic phase. Accordingly, the magnetic behavior of the film should show rather conventional FM behavior and reversal [44,45]. At sufficiently low temperatures,  $T_3 < T_C^G$ , shown in cyan in Fig. 1, the complete structure should be in its ferromagnetic state and exhibit a collective magnetization reversal as well, even if the film has a nonhomogeneous exchange profile, because  $T < T_C^{\text{loc}}(z)$  for all depths  $z$ . However, for intermediate temperatures,  $T_C^G < T_2 < T_C^T$ , shown in purple in Fig. 1, the film is designed to exhibit two separated FM regions, the magnetizations of which could, in principle, switch independently from each other.

The key strategy of this specifically designed EGP is that the separated FM regions at  $T = T_2$  can, in principle, interact with each other due to proximity effects. Hereby, the interaction should strongly depend on the thickness and properties of the PM spacer region, and thus, also on its precise temperature [47,50,51]. Furthermore, the gradient nature of  $T_C^{\text{loc}}(z)$  should lead to a continuous temperature-dependent change in the effective thickness of the PM portion separating both FM phases. Thus, the influence of the FM portions on each other can be expected to be strongly temperature dependent. It is worthwhile mentioning that it is far from clear if local variations of magnetization on the 1–2-nm length scale are actually compatible with current MRAM device designs, in which the magnetic layers themselves have total thicknesses of only about 1–2 nm. Nonetheless, our approach is far more likely to be compatible with other recently proposed designs, such as out-of-plane MTJ (pMTJ) MRAM devices, that rely on thicker magnetic layers [52].

To fabricate samples with such  $T_C^{\text{loc}}(z)$  profiles, we employ epitaxial  $\text{Co}_{1-x(z)}\text{Ru}_{x(z)}$  (10̄10) alloy films and vary the concentration,  $x$ , of Ru along the growth direction,  $z$ . Preliminary studies on homogeneous Co-Ru (10̄10) thin films show that  $T_C$  decreases in a nearly linear fashion as a function of  $x$  due to the corresponding decrease in the effective exchange energy [53,54], which allows us to accurately tailor the local magnetic properties of graded films [44,46]. In Fig. 2(a), we show in blue the specific  $x(z)$  pattern of Ru concentration as a function of depth for the type of films that we fabricate and, in red, the expected  $T_C^{\text{loc}}$  versus  $z$  dependence associated with our designed concentration profile, based on preliminary studies of homogeneous Co-Ru alloys [52,53].

Hereby, we choose the base layer to exhibit a high Curie temperature,  $T_C^B = 600$  K, such that its magnetic state is fairly constant over the temperature range of  $T = 100$ –300 K, in which the top portion of the film starts to order magnetically, and the specific properties of this

particular EGP become relevant [55]. In addition, we fabricate our films to have  $T_C^T = 225$  K and  $T_C^G = 150$  K, so that the temperature evolution in the different magnetic regimes can be well observed with our magnetometer.

The choice of epitaxial Co-Ru (10̄10) thin films is associated with the strong in-plane uniaxial magnetic anisotropy, which favors the formation of an easy magnetization axis (EA) along the [0001] direction within the surface plane [52,53]. Under such conditions, magneto-static interactions are essentially immaterial, and laterally uniform magnetization states occur, which enable a quantitatively accurate interpretation of macroscopic magnetization properties [52,53,56,57]. In such epitaxial films with strong in-plane uniaxial anisotropy, one commonly observes abrupt magnetization reversals as a function of the applied field in conventional magnetometer measurements, which are triggered by the formation of nucleation domains and progress subsequently via rapid domain-wall propagation [58]. Given the specific alloy used for our samples here, it is important to highlight that similar EGPs can be fabricated with a wide variety of alloy combinations, such as Ni-Cu [42] and Co-Cr [55] films, for instance, and thus, our alloy choice merely represents an example of such films and is meant to be an illustration of their fundamental behavior and design capabilities [53].

Furthermore, it is relevant to consider that, in principle, unintended intermixing of Ru and Co atoms can occur throughout the depth of the film, which would then lead to substantial modifications of the expected  $T_C^{\text{loc}}(z)$  profile. It is therefore important to mention that we are using a room-temperature deposition process to avoid such unintended intermixing and that, by means of polarized neutron reflectometry, we verify in samples, which are very similar to the ones we fabricate here, the existing compositional depth profiles are indeed the intended nominal profiles on the relevant length scale, given that unintended intermixing is limited to below 2 nm in depth [43,59]. Thus, while certain intermixing can occur, it is limited to length scales that are smaller than the magnetically relevant profile features of our films.

In Fig. 2(b), we show a schematic of the specific multilayer sequence employed for the growth of our Co-Ru (10̄10) films. We fabricate our samples by means of sputter deposition utilizing an UHV system (ATC Series AJA International) with a base pressure better than  $10^{-8}$  mTorr. On top of hydrofluoric-acid-etched, and thus, oxide-removed Si (110) wafers, we deposit a specific underlayer sequence composed of 75-nm Ag (110), 20-nm Cr (211), and 20-nm  $\text{Cr}_{0.86}\text{Ru}_{0.14}$  (211) films [53] that allows for the high-quality epitaxial growth of magnetic  $\text{Co}_{1-x(z)}\text{Ru}_{x(z)}$  (10̄10) film. 10-nm-thick  $\text{SiO}_2$  overcoat layers are added at the end of the deposition process to protect our  $\text{Co}_{1-x(z)}\text{Ru}_{x(z)}$  films from oxidation. The  $\text{Co}_{1-x(z)}\text{Ru}_{x(z)}$  layers themselves are fabricated by cosputter deposition of Co and Ru, in which the deposition

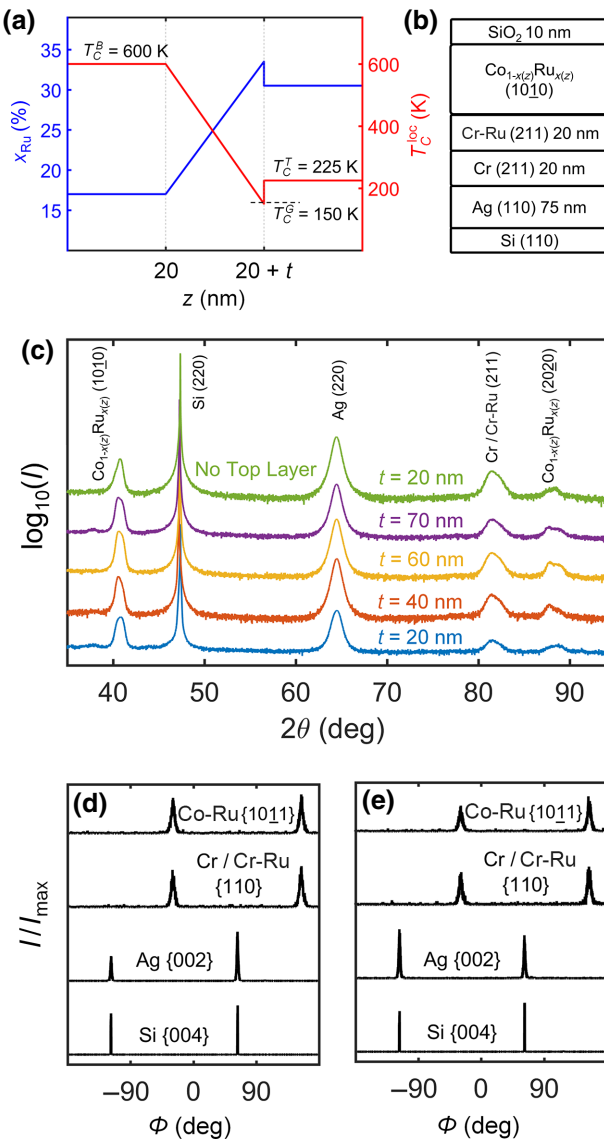


FIG. 2. (a) Experimental Ru concentration as a function of sample depth,  $z$ , employed in our multilayer structures (blue) and associated  $T_C^{\text{loc}}$  (red) profiles estimated from preliminary studies of homogeneous films. (b) Schematic of the multilayer structure employed in our films to achieve epitaxial growth of the  $\text{Co}_{1-x(z)}\text{Ru}_{x(z)}$  (1010) layers. (c) XRD  $\theta$ - $2\theta$  scans of our films with graded coupling-layer thicknesses,  $t$ , ranging from 20 to 70 nm, and a reference sample without a top layer for  $t=20$  nm. Observed XRD peaks are indexed. (d),(e) XRD azimuthal scans at the  $2\theta$  poles of  $\text{Si}$  {004},  $\text{Ag}$  {002},  $\text{Cr}$  {110}, and  $\text{Co-Ru}$  {1011} for the  $t=20$  and 40 nm samples, respectively.

rate of Co is adjusted during growth to facilitate the growth profile shown in Fig. 2(a). In Fig 2(c), we show x-ray diffraction (XRD)  $\theta$ - $2\theta$  scans for each of our so-fabricated films, representing different values of thickness,  $t$ , for the graded coupling layer. We also fabricate a reference sample without a top magnetic layer and  $t=20$  nm to elucidate the top layer's role in the overall behavior

of our EGP films. In Fig. 2(c), we observe only diffraction peaks corresponding to the intended crystallographic planes for each of the deposited layers. The presence of the Co-Ru (2020) second-order peaks and the absence of peaks corresponding to other crystallographic orientations verify the high quality of our EGP film samples. The peaks corresponding to Co-Ru (1010) and Co-Ru (2020) show a certain level of broadening and/or splitting due to the continuous alloy-composition-induced modification of the lattice spacing along the depth of the film, which is another good indication that epitaxy is maintained throughout the entire depth. Given that the maximum and minimum Ru concentrations are kept constant in all films, no relevant shift is expected for these peaks as a function of  $t$ , which is exactly what we observe.

Figures 2(d) and 2(e) show exemplarily two XRD azimuthal  $\phi$  scans for the samples with  $t=20$  and 40 nm, respectively. These measurements are performed at crystal planes that are not perpendicular to the film surface, which provides information about the in-plane crystal structure and relative orientations between layers in our films. In Figs. 2(d) and 2(e), we show the x-ray intensity, normalized to the maximum value in each corresponding measurement. All our  $\phi$  scans show two well-defined peaks that are  $180^\circ$  apart with positions that match the stereographic projections of their nominal structure [55,60]. The  $\text{Si}$  {004} and  $\text{Ag}$  {002} scans indicate a parallel alignment of the  $\text{Si}$  and  $\text{Ag}$  [001] directions. At the same time, the  $90^\circ$  angular shift between the  $\text{Ag}$  and  $\text{Cr/Cr-Ru}$  peaks indicates that the  $\text{Cr}$  [110] direction is parallel to the  $\text{Ag}$  [001] direction, as intended. Finally, the Co-Ru peaks appear at the same  $\phi$  values as those for  $\text{Cr}$  {110}, confirming the in-plane alignment of the Co-Ru [0001] direction, and thus, unambiguously verifying the epitaxial nature of our films.

### III. MAGNETIC CHARACTERIZATION

We conduct temperature-dependent magnetometry measurements using a superconductive quantum-interference device (SQUID) (Quantum Design MPMS SQUID-VSM) for the purpose of measuring the hysteresis loops of our EGP film samples in the temperature range of  $T=100$ –300 K. Specifically, we measure the magnetization component parallel to the field, applied in-plane and parallel to the magnetic easy axis of our samples. In Fig. 3, we show three exemplary hysteresis loops at three different temperatures for our full EGP sample with  $t=20$  nm. In Figs. 3(a) and 3(c), we observe nearly perfect square-like hysteresis loops at  $T=100$  and 280 K, respectively, showing only a single abrupt magnetization reversal at  $H_c$ , as one would expect for a conventional uniaxial magnetic film along its EA. In Fig. 3(a), the complete structure exhibits a FM state at all depths because  $T < T_C^G$ , which is equivalent to the case of  $T_3$  in Fig. 1. On the other hand, in Fig. 3(c), only the base layer and part of the graded

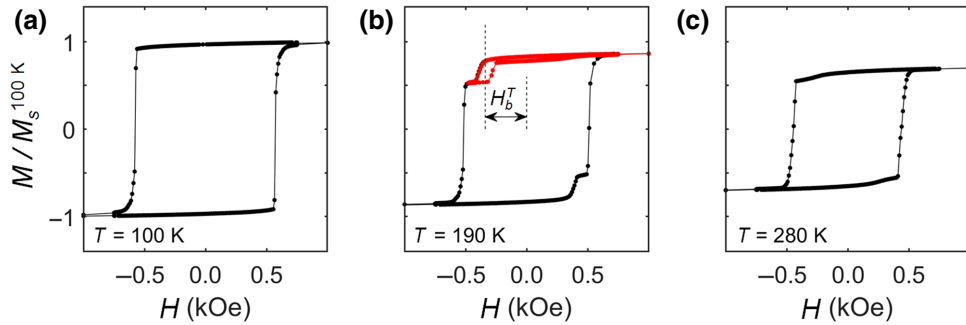


FIG. 3. Exemplary normalized hysteresis loops measured for the  $t = 20$  nm EGP sample at (a) 100 K, (b) 190 K, and (c) 280 K. Red line in (b) represents a minor hysteresis loop, exhibiting a strong bias field,  $H_b^T$ , on the top layer.

coupling layer are in a FM state because  $T_C^T < T < T_C^B$ . Therefore, the film shows typical single-film behavior for these two different temperature regimes, even if  $T_C^{\text{loc}}(z)$  is not constant. We also observe a decrease of the total magnetic moment in Fig. 3(c) due to the fact that a large portion of the film is not ferromagnetic at  $T = 280$  K.

For intermediate temperatures, as shown in Fig. 3(b), the abrupt reversal at  $H_c$  is still present, but, in addition, we observe that the hysteresis loop exhibits a two-step reversal process. This double step is due to the formation of two separated FM regions at intermediate temperatures that can switch independently, as explained in conjunction with Fig. 1. The first small step corresponds to the reversal of the top layer alone, which is ferromagnetically ordered at this temperature. The contribution to the total moment of this layer is smaller, given that this portion of the film has a  $T_C^{\text{loc}}$  close to  $T$ , whereas the larger step corresponds to the reversal of the bottom FM layer and the adjacent part of the graded coupling layer, which is ferromagnetically ordered as well. To test for possible exchange coupling between the two separate ferromagnetic segments of our EGP films at intermediate temperatures, we measure minor hysteresis loops of the top magnetic layer only, shown comparatively in red in Fig. 3(b). For this purpose, we start at sufficiently high positive magnetic fields and decrease the field down to a value at which only the top FM layer has reversed and, then, we increase the field again to observe the full hysteretic behavior of the top FM layer. Here, we clearly observe that the hysteresis loop of the top region is shifted with respect to  $H = 0$ , which verifies the existence of a significant ferromagnetic bias field,  $H_b^T$ , that is mediated by the paramagnetic state of the interlayer in the vicinity of the top layer. This behavior is in accordance with the intended magnetic properties of this specific EGP film structure explained by Fig. 1. It is important to also highlight that reversal of the FM portion of the graded coupling layer cannot be resolved on its own with our SQUID magnetometer, given that it forms a collective FM state jointly with the bottom FM layer, in the very same way in which the top layer forms a collective FM state with the rest of the

film at sufficiently low temperatures ( $T < T_C^G$ ), at which a full depth correlation of the FM state is established.

To study the process of magnetization reversal in our films in detail, we measure hysteresis loops every 2 K over the full 100–300 K temperature range. In Fig. 4(a), we display the total moment,  $m$ , as a function of  $T$  and  $H$  for the  $t = 20$  nm film sample as a color-coded map, representing the decreasing field branch of the hysteresis loop. Data are obtained at each  $T$  value by decreasing the field from saturation at  $H = 2$  kOe. In this color map, we can identify a nearly abrupt magnetization reversal at sufficiently large negative field values for all temperatures, represented in the color map by the narrow yellow regions, which correspond to zero magnetization and separate the positive (blue) and negative (red) moment values. For intermediate temperatures, we also identify a blue-to-green transition, which represents the second magnetization-reversal step of the top layer, which is explained in conjunction with Fig. 3(b). Thus, the green region of the map represents the antiparallel alignment of the two FM regions of the film. In this map, we also observe that the coercive field, at which sample magnetization completely inverts to negative values, does not change monotonously but, instead, contains a very significant temperature region, in which  $H_c$  remains basically constant. Furthermore, this temperature region of constant  $H_c$  fully coincides with the temperature range over which we observe the double step reversal.

In Fig. 4(b), we explicitly plot the experimentally determined  $H_c$  versus  $T$  behavior, which one can already visualize in Fig. 4(a) as a light-yellow line in the data map for the  $t = 20$  nm sample, in comparison to the behavior of the reference sample without a top layer. Here, we can clearly identify the very wide temperature “plateau” of constant coercivity, in which relative coercivity changes of less than 2% extend over a temperature range of 75 K, as indicated by the vertical dashed lines in Fig. 4(b). In contrast, measurements of our reference sample display very conventional behavior, exhibiting about 20% coercivity change over the exact same temperature range, as well as an overall monotonous  $H_c$  versus  $T$  characteristic

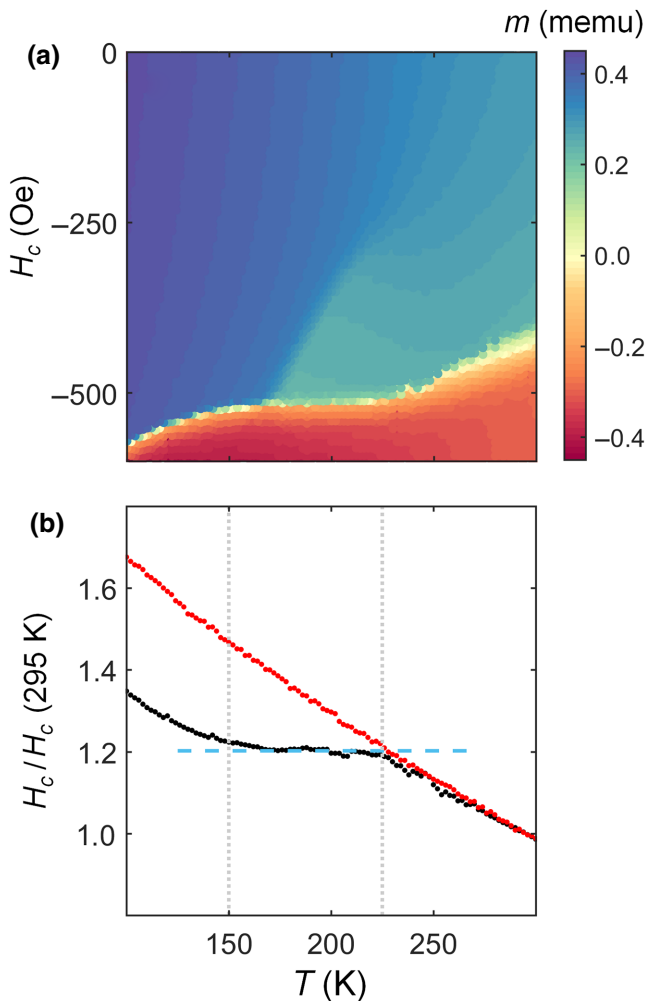


FIG. 4. (a) Color-coded map of experimentally measured total sample magnetization as a function of  $T$  and  $H$  for the EGP film sample with  $t = 20$  nm. Data are obtained for decreasing field sequences, each for a fixed  $T$  value. Color bar on the right-hand side represents the values of total moment. (b) Experimental  $H_c$  versus  $T$  data normalized to their room-temperature values for the  $t = 20$  nm EGP film (black) and the reference film sample without a top layer (red). Gray dashed vertical lines represent the temperature range over which two separate FM entities coexist, and light-blue dashed horizontal line represents the constant coercivity over this specific temperature range.

at all temperatures. Also, it is important to notice that our EGP sample exhibits a fairly conventional  $H_c$  versus  $T$  behavior outside the plateau region, namely, at low and high temperatures. These results verify that the observed constant-coercivity plateau is due to the interaction of the top FM layer with the bottom FM section of the film. This behavior can be understood if one considers that the top FM layer also induces a temperature-dependent bias onto the bottom FM region in our EGP film, which counteracts the conventional temperature increase of  $H_c$  upon lowering  $T$ . Thus, we successfully design FM films from rather

conventional ferromagnetic alloy materials that exhibit constant coercivity within a designed temperature range by utilizing the EGP strategy.

Figure 5 displays the  $H_c(T)$  behavior for a series of samples, in which the thickness,  $t$ , of the graded layer segment is varied. In all cases, we clearly observe three different  $H_c$  regimes, corresponding to the three temperature ranges defined in Fig. 1 and similar to the behavior observed for the  $t = 20$  nm case in Fig. 4. The central temperature range has a significantly reduced  $H_c(T)$  dependence due to the interaction with the top layer in all the cases explored here. We also note that the overall observed  $H_c$  values decrease in a rather monotonous manner with  $t$  because  $H_c$  is fundamentally related to the strong anisotropy in the base layer, and this becomes a decreasing volume fraction of our multilayer structure as  $t$  increases.

The influence of the top magnetic layer on the reversal is most notable in the  $t = 20$  nm film, as shown in Fig. 4. Thus, while a temperature-dependent bias is observable in all of the cases explored here, we obtain a plateau of constant coercivity only in the  $t = 20$  nm case because only in this case is the bias impact of the top magnetic region sufficiently large to fully compensate for the intrinsic  $H_c(T)$  dependence of the bottom FM region. This observed  $t$  dependence is consistent with our expectation that the interlayer coupling is weaker for thicker paramagnetic layers, which exist for larger  $t$  values.

#### IV. MODEL EXPLANATION

To achieve an in-depth understanding of the reversal process and its temperature dependence in our EGP films, we develop a basic model based on the crucial step of magnetic reversal nucleation within the bottom FM portion of the film. Hereby, we assume that, when a sufficiently stable reversal domain has nucleated, the full magnetization reversal of this layer proceeds rapidly on the timescale of our experiments by means of domain-wall propagation, leading to the observed sharp  $M$  versus  $H$  switch at  $H_c$  [57]. The formation probability,  $P$ , of a stable nucleation domain that triggers this magnetization reversal can be written by means of an Arrhenius law of the form [61]

$$P = p_0 e^{-E_B/k_B T}. \quad (1)$$

Hereby,  $p_0$  is a temperature-independent material-specific constant,  $E_B$  is the activation-energy barrier, and  $k_B T$  is the thermal energy. The activation energy barrier in our system describes the total energy required for the formation of a sufficiently stable reversal nucleation domain of volume  $V_B$  that will trigger the reversal. Hereby,  $E_B$  can be expressed as a sum of three energy terms as

$$E_B = \varepsilon_{\text{DW}} A_{\text{DW}} - 2HM_B V_B - 2J(T)A_N \frac{M_B}{M_B^S} \frac{M_T}{M_T^S}. \quad (2)$$

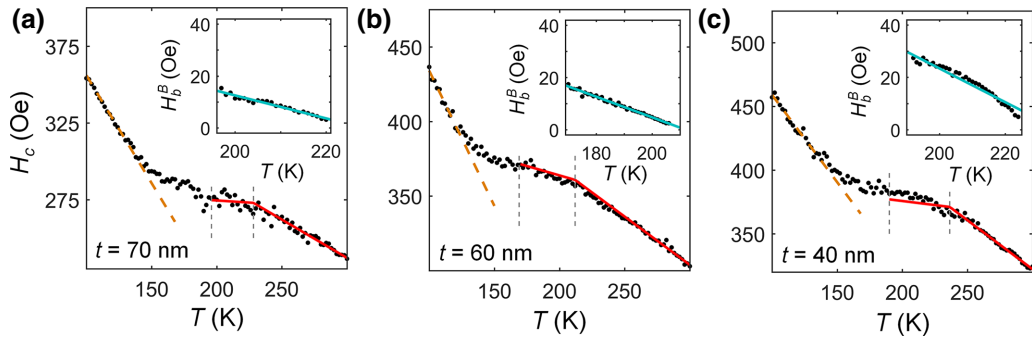


FIG. 5. Experimental  $H_c$  data as a function of  $T$  (black dots) for samples with  $t =$  (a) 70, (b) 60, and (c) 40 nm. Red line represents our model behavior, and dashed vertical lines represent the  $T$  range, in which minor hysteresis loops of the top layer are visible. Orange-dashed lines represent model behavior at low temperatures. Insets represent the experimentally obtained  $H_b^B$  versus  $T$  behavior determined from minor-loop measurements. Light-blue lines in the insets represent the linear fitting of these data.

The first term on the right-hand side is the nucleation energy associated with the energy cost of having a domain wall with energy density  $\varepsilon_{\text{DW}}$  and area  $A_{\text{DW}}$ . The second is the Zeeman energy gain of the nucleation domain in the bottom portion of the film with magnetization  $M_B$ . The last term in Eq. (2) represents the energy contribution from the interlayer exchange coupling between the two FM regions in the film. Specifically,  $J(T)$  is the effective interlayer-exchange-coupling energy density per unit area that is mediated by the paramagnetic portion of the graded coupling layer in the area,  $A_N$ , of the nucleation domain.  $M_T$  is the magnetization of the top layer, and  $M_B^S$  and  $M_T^S$  are the saturation magnetizations of the bottom and top portions of the film, respectively. This third energy contribution represents proximity effects in between the FM portions of the film that are mediated by the interlayer. Near the FM/PM interfaces, the magnetization profile inside the PM interlayer exhibits an exponential fall off on the nanometer-length scale [62], which ultimately results in a small, but nonvanishing, interaction between the FM regions [63]. This proximity effect is actually present at both interfaces at which the FM sample state borders a PM state, i.e., both at the interface between the graded and top layer, as well as within the graded segment at the very point at which  $T_C^{\text{loc}}$  is identical to the measurement temperature,  $T$ , and with  $T - T_C^{\text{loc}}$  defining the exponential decay length within the PM region in either case [61,64].

In our films,  $J(T)$  is a nonlinear function that depends on the effective thickness of the intermediate PM region, and it is expected to vary with temperature. However, we note that we can actually extract the information of this interlayer energy term from our minor-loop measurements of the top layer. This is because this energy term can be described by an effective bias field,  $H_b^B$ , acting on  $M_B$ , and equivalently,  $H_b^T$  acting on  $M_T$  as

$$J(T)A_N \frac{M_B M_T}{M_B^S M_T^S} = H_b^B M_B V_B = H_b^T M_T V_T. \quad (3)$$

Therefore, Eq. (3) gives us a relationship between  $H_b^B$  and  $H_b^T$  that allows us to calculate the effective  $H_b^B$  from the experimental  $H_b^T$  data, which we obtain from minor-loop measurements of the top layer, as shown exemplary in Fig. 3(b).

Using this model approach, we can consider that the nucleation and domain-wall expansion that leads to magnetization reversal gets triggered at  $P = 1$ , meaning that a domain with a reversed magnetization state forms and expands. Thus, combining Eqs. (1)–(3), we obtain

$$H_c(T) = H_c(0) - \alpha T - H_b^B(T), \quad (4)$$

where  $H_c(0) = A_{\text{DW}} \varepsilon_{\text{DW}} / 2M_B V_B$  and  $\alpha = k_B \ln(p_0) / 2M_B V_B$ . Due to the fact that  $M_B$  is only varying slowly in the 100–300 K temperature range, given that  $T_C^B = 600$  K, and under the assumption that all geometric factors are only weakly temperature dependent as well, the first two terms in Eq. (4) predict an approximately linear decrease of  $H_c$  as a function of  $T$ , which is basically the behavior observed in our reference sample in Fig. 4(b), and the behavior of all of our samples in the high- $T$  and low- $T$  regimes.

In the insets of Fig. 5, we show the  $H_b^B(T)$  data determined based on our minor-loop measurements. Here, we clearly observe the existence of a bias field acting upon the bottom portion of the film in the central temperature range in all our samples. Furthermore, these  $H_b^B(T)$  curves have a strong temperature dependence that counteracts the conventional  $H_c(T)$  behavior, as expected. The light-blue lines represent linear least-squares fits to experimental data, illustrating that  $H_b^B(T)$  behaves in an almost linear fashion with a slope  $\alpha_b$ . For different samples, we observe, as expected, that  $\alpha_b$  in the  $H_b^B(T)$  curves is larger for smaller EGP thickness  $t$ , because the influence of the top layer on the bottom portion of the film will be greater for smaller thicknesses of the effective PM region. This behavior verifies that one can compensate for the conventional  $H_c$  versus  $T$  dependence at will by making a suitable choice of the thickness of the graded coupling layer.

TABLE I. Numerical results of the fitting procedures showing the  $H_c(T)$  behavior in our samples at low and high temperatures, together with those of the  $H_b(T)$  behavior.

$t$ (nm)	High $T$		Bias		Low $T$	
	$\alpha$ (Oe/K)	$H_c(0)$ (K)	$\alpha_b$ (Oe/K)	$H_b^B(0)$ (K)	$\alpha$ (Oe/K)	$H_c(0)$ (K)
20	$-1.09 \pm 0.06$	$748 \pm 10$	$-1.08 \pm 0.08$	$257 \pm 10$	$-1.3 \pm 0.10$	$711 \pm 10$
40	$-0.77 \pm 0.05$	$553 \pm 10$	$-0.64 \pm 0.06$	$150 \pm 10$	$-1.3 \pm 0.10$	$597 \pm 10$
60	$-0.65 \pm 0.04$	$498 \pm 10$	$-0.39 \pm 0.02$	$83 \pm 3$	$-1.8 \pm 0.20$	$616 \pm 20$
70	$-0.49 \pm 0.04$	$384 \pm 10$	$-0.44 \pm 0.04$	$101 \pm 9$	$-1.31 \pm 0.06$	$485 \pm 6$

In Fig. 5, the red lines show the model behavior of Eq. (4). Here, we consider a linear expansion at high temperatures, which represent the first two energy terms in Eq. (4). In the  $T$  range, in which the minor loops can be observed, and which is identified by means of the gray-dashed vertical lines, we add the  $H_b^B(T)$  data, which represent the third term in Eq. (4). We note that the model explains the  $H_c(T)$  behavior very well for all of our samples in Fig. 5 over the temperature range at which minor loops are measured. The numerical results of these fits are shown in Table I. Here, we show our fitting results of the low- and high-temperature expansions, together with the linear fitting of the  $H_b^B(T)$  curve. Here, we verify that  $\alpha_b$  increases for decreasing thickness of the graded coupling layer, and thus, we verify that our simple model captures the essence of the experimentally observed behavior. Furthermore, we observe that, at  $t = 20$  nm,  $\alpha_b$  is basically identical to  $\alpha$  at high temperatures, which leads to the compensation effect that creates the coercivity plateau. These results identify the interlayer exchange coupling via the paramagnetic graded-layer portion as the key mechanism that facilitates the intended  $H_c(T)$  modification and explains, in a quantitatively accurate manner, the overall magnetization-reversal process. For the lowest temperatures, the complete EGP structure exhibits a strongly coupled single FM phase, leading to the reemergence of linear  $H_c(T)$  behavior, as shown by the dashed orange lines in Fig. 5.

## V. CONCLUSIONS

In this work, we study magnetization reversal in thin films with specifically designed exchange-gradient profiles on the nanometer scale that enable the realization of very wide temperature regions, in which such films exhibit constant coercivities, in contrast to similar homogeneous alloy samples. We show that we can construct films in which  $H_c$  changes less than 2% over a 75-K-wide temperature plateau, while conventional films exhibit coercivity changes of 20%. Our detailed magnetometry study furthermore explains this behavior, in that the temperature dependence of the effective PM spacer layer in our design leads to strongly temperature-dependent bias fields that oppose the conventionally occurring  $H_c$  changes with temperature. While the temperature region of our

$H_c$  plateau is chosen for experimental convenience, this plateau region can be designed for any temperature range, so that possible applications and devices that use a specific temperature range for their operation can be accommodated. Furthermore, our overall experimental results demonstrate that a wide variety of different temperature dependencies of  $H_c$  can be engineered by means of a suitable choice of graded-layer thickness and the specific  $T_C^{\text{loc}}(z)$  profile.

In general, our work here constitutes a proof-of-concept of the capabilities of specifically designed exchange-graded ferromagnets for controlling temperature-dependent bias fields, and thus, coercivity. However, there could be a number of practical limitations to our particular sample design and material choice. First, nonmagnetic impurities generally lead to an increase of the Gilbert damping constant, which is detrimental to the performance of devices [65,66]. Nonetheless, proposals in the literature also predict an improved spin-wave channeling in graded materials that can be beneficial for device designs [67].

Also, commercial MRAM devices generally employ Co-Fe-B/MgO multilayers, in which the spin polarization and magnetoresistance signals are larger. In this context, it is important to mention that our methodology here is general and can be utilized for many different kinds of ferromagnetic materials and applications, either with higher or lower  $H_c$  values, and with a great deal of flexibility in choosing the most relevant temperature-range target. Thus, it could be interesting to explore, for example, the capabilities of graded compositions of different materials on the Co-Fe-B/MgO multilayers mentioned [63,68], which could have a strong influence on the thermal stability and reliability of next-generation devices.

## ACKNOWLEDGMENTS

Our work is supported by the Spanish Ministry of Science and Innovation under the Maria de Maeztu Units of Excellence Programme (Grant No. CEX2020-001038-M) and Project No. RTI2018-094881-B-100 (MCIU/Feder), as well as by Predoctoral Fellowship No. PRE2019-088428. C.M.V. acknowledges the Basque Government for support from Fellowship No. PRE\_2021\_1\_0056.

- [1] R. Skomski, Nanomagnetics, *J. Phys.: Condens. Matter* **15**, R841 (2003).
- [2] O. Gutfleisch, M. A. Willard, E. Brück, C. H. Chen, S. G. Sankar, and J. P. Liu, Magnetic materials and devices for the 21st century: Stronger, lighter, and more energy efficient, *Adv. Mater.* **23**, 821 (2011).
- [3] E. Y. Vedmedenko, R. K. Kawakami, D. D. Shenka, P. Gambardella, A. Kirilyuk, A. Hirohata, C. Binek, O. Chubykalo-Fesenko, S. Sanvito, B. J. Kirby, *et al.*, The 2020 magnetism roadmap, *J. Phys. D: Appl. Phys.* **53**, 453001 (2020).
- [4] H. T. Nembach, P. Martín Pimentel, S. J. Hermsdoerfer, B. Leven, and B. Hillebrands, Microwave assisted switching in a Ni<sub>81</sub>Fe<sub>19</sub> ellipsoid, *Appl. Phys. Lett.* **90**, 062503 (2007).
- [5] F. J. Albert, J. A. Katine, and R. A. Buhrman, Spin-polarized current switching of a Co thin film nanomagnet, *Appl. Phys. Lett.* **77**, 3809 (2000).
- [6] N. D. Goldenfeld, *Lectures on Phase Transitions and the Renormalization Group* (Addison-Wesley, Reading, MA, 1992).
- [7] G. V. Brown, Magnetic heat pumping near room temperature, *J. Appl. Phys.* **47**, 3673 (1976).
- [8] A. Fujita, S. Fujieda, Y. Hasegawa, and K. Fukamichi, Itinerant-electron metamagnetic transition and large magnetocaloric effects in La(Fe<sub>x</sub>Si<sub>1-x</sub>)<sub>13</sub> compounds and their hydrides, *Phys. Rev. B* **67**, 104416 (2003).
- [9] J. Liu, T. Gottschall, K. P. Skokov, J. D. Moore, and O. Gutfleisch, Giant magnetocaloric effect driven by structural transitions, *Nat. Mater.* **11**, 620 (2012).
- [10] M. Balli, S. Jandl, P. Fournier, and A. Kedous-Lebouc, Advanced materials for magnetic cooling: Fundamentals and practical aspects, *Appl. Phys. Rev.* **4**, 021305 (2017).
- [11] A. Talaat, M. V. Suraj, K. Byerly, A. Wang, Y. Wang, J. K. Lee, and P. R. Ohodnicki Jr., Review on soft magnetic metal and inorganic oxide nanocomposites for power applications, *J. Alloys Compd.* **870**, 159500 (2021).
- [12] J. M. Silveyra, E. Ferrara, D. L. Huber, and T. C. Monson, Soft magnetic materials for a sustainable and electrified world, *Science* **362**, 6413 (2018).
- [13] J. M. D. Coey, Hard magnetic materials: A perspective, *IEEE Trans. Magn.* **47**, 4671 (2011).
- [14] M. H. Kryde, E. C. Gage, T. W. McDaniel, W. A. Challener, R. E. Rottmayer, G. Ju, Y.-T. Hsia, and M. F. Erden, Heat assisted magnetic recording, *Proc. IEEE* **96**, 1810 (2008).
- [15] S. N. Piramanayagam and K. Srinivasan, Recording media research for future hard disk drives, *J. Magn. Magn. Mater.* **321**, 485 (2009).
- [16] R. Wood, Future hard disk drive systems, *J. Magn. Magn. Mater.* **321**, 555 (2009).
- [17] K. H. J. Buschow, New developments in hard magnetic materials, *Rep. Prog. Phys.* **54**, 1123 (1991).
- [18] H. R. Kirchmayr, Permanent magnets and hard magnetic materials, *J. Phys. D: Appl. Phys.* **29**, 2763 (1996).
- [19] S. Ikeda, K. Miura, H. Yamamoto, K. Mizunuma, H. D. Gan, M. Endo, S. Kanai, J. Hayakawa, F. Matsukura, and H. Ohno, A perpendicular-anisotropy CoFeB–MgO magnetic tunnel junction, *Nat. Mater.* **9**, 721 (2010).
- [20] J. M. Iwata-Harms, G. Jan, H. Liu, S. Serrano-Guisan, J. Zhu, L. Thomas, R.-Y. Tong, V. Sundar, and P.-K. Wang, High-temperature thermal stability driven by magnetization dilution in CoFeB free layers for spin-transfer-torque magnetic random access memory, *Sci. Rep.* **8**, 14409 (2018).
- [21] V. Krizakova, E. Grimaldi, K. Garello, G. Sala, S. Couet, G. Sankar Kar, and P. Gambardella, Interplay of Voltage Control of Magnetic Anisotropy, Spin-Transfer Torque, and Heat in the Spin-Orbit-Torque Switching of Three-Terminal Magnetic Tunnel Junctions, *Phys. Rev. Appl.* **15**, 054055 (2021).
- [22] Y. C. Wu, K. Garello, W. Kim, M. Gupta, M. Perumkunnil, V. Kateel, S. Couet, R. Carpenter, S. Rao, S. Van Beek, *et al.*, Voltage-Gate-Assisted Spin-Orbit-Torque Magnetic Random-Access Memory for High-Density and Low-Power Embedded Applications, *Phys. Rev. Appl.* **15**, 064015 (2021).
- [23] Y. Takeuchi, E. C. I. Enobio, B. Jinnai, H. Sato, S. Fukami, and H. Ohno, Temperature dependence of intrinsic critical current in perpendicular easy axis CoFeB/MgO magnetic tunnel junctions, *Appl. Phys. Lett.* **119**, 242403 (2021).
- [24] H. Sato, E. C. I. Enobio, M. Yamanouchi, S. Ikeda, S. Fukami, S. Kanai, F. Matsukura, and H. Ohno, Properties of magnetic tunnel junctions with a MgO/CoFeB/Ta/CoFeB/MgO recording structure down to junction diameter of 11 nm, *Appl. Phys. Lett.* **105**, 062403 (2014).
- [25] L. Zhang, Y. Cheng, W. Kang, L. Torres, Y. Zhang, A. Todri-Sanial, and W. Zhao, Addressing the thermal issues of STT-MRAM from compact modeling to design techniques, *IEEE Trans. Nanotechnol.* **17**, 345 (2018).
- [26] N. Dwivedi, A. K. Ott, K. Sasikumar, C. Dou, R. J. Yeo, B. Narayanan, U. Sassi, D. De Fazio, G. Soavi, T. Dutta, *et al.*, Graphene overcoats for ultra-high storage density magnetic media, *Nat. Commun.* **12**, 2854 (2021).
- [27] R. C. Sousa, M. Kerekes, I. L. Prejbeanu, O. Redon, B. Dieny, J. P. Nozières, and P. P. Freitas, Crossover in heating regimes of thermally assisted magnetic memories, *J. Appl. Phys.* **99**, 08N904 (2006).
- [28] K. Watanabe, B. Jinnai, S. Fukami, H. Sato, and H. Ohno, Shape anisotropy revisited in single-digit nanometer magnetic tunnel junctions, *Nat. Commun.* **9**, 663 (2018).
- [29] B. Jinnai, K. Watanabe, S. Fukami, and H. Ohno, Scaling magnetic tunnel junction down to single-digit nanometers—challenges and prospects, *Appl. Phys. Lett.* **116**, 160501 (2020).
- [30] Y. C. Wu, W. Kim, S. Van Beek, S. Couet, R. Carpenter, S. Rao, S. Kundu, J. Van Houdt, G. Groeseneken, D. Crotti, and G. S. Kar, Impact of ambient temperature on the switching of voltage-controlled perpendicular magnetic tunnel junction, *Appl. Phys. Lett.* **118**, 122404 (2021).
- [31] X. Fan, K. Chen, S. Guo, R. Chen, D. Lee, A. Yan, and C. You, Core-shell Y-substituted Nd–Ce–Fe–B sintered magnets with enhanced coercivity and good thermal stability, *Appl. Phys. Lett.* **110**, 172405 (2017).
- [32] J. S. Zhang, L. Z. Zhao, X. F. Liao, H. X. Zeng, D. R. Peng, H. Y. Yu, X. C. Zhong, and Z. W. Liu, Suppressing the CeFe<sub>2</sub> phase formation and improving the coercivity and thermal stability of Ce–Fe–B alloys by Si substitution, *Intermetallics* **107**, 75 (2019).
- [33] G. Ding, S. Liao, J. Di, B. Zheng, S. Guo, R. Chen, and Ara Yam, Microstructure of core-shell NdY–Fe–B sintered magnets with a high coercivity and excellent thermal stability, *Acta Mater.* **194**, 547 (2020).

- [34] J.-U. Thiele, S. Maat, J. L. Robertson, and E. E. Fullerton, Magnetic and structural properties of FePt-FeRh exchange spring films for thermally assisted magnetic recording media, *IEEE Trans. Magn.* **40**, 2537 (2004).
- [35] D. Suess, T. Schrefl, S. Fähler, M. Kirschner, G. Hrkac, F. Dorfbauer, and J. Fidler, Exchange spring media for perpendicular recording, *Appl. Phys. Lett.* **87**, 012504 (2005).
- [36] V. Neu, K. Häfner, and L. Schultz, Dynamic coercivity and thermal stability of epitaxial exchange spring trilayers, *J. Magn. Magn. Mater.* **322**, 1613 (2010).
- [37] A. Berger, N. Supper, Y. Ikeda, B. Lengsfeld, A. Moser, and E. E. Fullerton, Improved media performance in optimally coupled exchange spring layer media, *Appl. Phys. Lett.* **93**, 122502 (2008).
- [38] W. Griggs, C. Bull, C. W. Barton, R. A. Griffiths, A. J. Caruna, C. J. Kinane, P. W. Nutter, and T. Thomson, Polarized neutron reflectometry characterization of interfacial magnetism in an FePt/FeRh exchange spring, *Phys. Rev. Mater.* **6**, 024403 (2022).
- [39] R. A. Gallardo, P. Alvarado-Seguel, T. Schneider, C. Gonzalez-Fuentes, A. Roldán-Molina, K. Lenz, J. Lindner, and P. Landeros, Spin-wave non-reciprocity in magnetization-graded ferromagnetic films, *New J. Phys.* **21**, 033026 (2019).
- [40] L. Fallarino, B. Kirby, and E. Fullerton, Graded magnetic materials, *J. Phys. D: Appl. Phys.* **54**, 303002 (2021).
- [41] Z. Zheng, Y. Zhang, V. Lopez-Dominguez, L. Sánchez-Tejerina, J. Shi, X. Feng, L. Chen, Z. Wang, Z. Zhang, K. Zhang, *et al.*, Field-free spin-orbit torque-induced switching of perpendicular magnetization in a ferrimagnetic layer with a vertical composition gradient, *Nat. Commun.* **12**, 4555 (2021).
- [42] B. J. Kirby, H. F. Belliveau, D. D. Belyea, P. A. Kienzle, A. J. Grutter, P. Riego, A. Berger, and C. W. Miller, Spatial Evolution of the Ferromagnetic Phase Transition in an Exchange Graded Film, *Phys. Rev. Lett.* **116**, 047203 (2016).
- [43] L. Fallarino, P. Riego, B. J. Kirby, C. W. Miller, and A. Berger, Modulation of magnetic properties at the nanometer scale in continuously graded ferromagnets, *Materials* **11**, 251 (2018).
- [44] L. Fallarino, E. López Rojo, M. Quintana, J. S. Salcedo Gallo, B. J. Kirby, and A. Berger, Modifying Critical Exponents of Magnetic Phase Transitions via Nanoscale Materials Design, *Phys. Rev. Lett.* **127**, 147201 (2021).
- [45] L. Fallarino, M. Quintana, E. López Rojo, and A. Berger, Suppression of Coercivity in Nanoscale Graded Magnetic Materials, *Phys. Rev. Appl.* **16**, 034038 (2021).
- [46] J. S. Salcedo Gallo, A. Berger, M. Quintana, E. Restrepo Parra, and L. Fallarino, Nanoscale control of temperature operation ranges for magnetocaloric applications, *J. Phys. D: Appl. Phys.* **54**, 304003 (2021).
- [47] A. F. Kravets, A. N. Timoshhevskii, B. Z. Yanchitsky, M. A. Bergmann, J. Buhler, S. Andersson, and V. Korenivski, Temperature-controlled interlayer exchange coupling in strong/weak ferromagnetic multilayers: A thermomagnetic Curie switch, *Phys. Rev. B* **86**, 214413 (2012).
- [48] D. M. Polishchuk, A. F. Kravets, Y. O. Tykhanenko-Polishchuk, A. I. Tovstolytkin, and V. Korenivski, Ferromagnetic resonance and interlayer exchange coupling in magnetic multilayers with compositional gradients, *AIP Advances* **7**, 056307 (2017).
- [49] A. F. Kravets, D. M. Polishchuk, V. A. Pashchenko, A. I. Tovstolytkin, and V. Korenivski, Current-driven thermomagnetic switching in magnetic tunnel junctions, *Appl. Phys. Lett.* **111**, 262401 (2017).
- [50] U. Gradmann, Magnetism of surfaces and interfaces, *J. Magn. Magn. Mater.* **6**, 173 (1977).
- [51] R. Weber, C. Martín Valderrama, L. Fallarino, and A. Berger, Dependence of the magneto-optical signal on the Co layer thickness asymmetry in Co/Pt/Co films, *Phys. Rev. B* **102**, 214434 (2020).
- [52] N. Perrissin, S. Lequeux, N. Strelkov, A. Chavent, L. Villa, L. D. Buda-Prejbeanu, S. Auffret, R. C. Sousa, I. L. Prejbeanu, and B. Dieny, A highly thermally stable sub-20 nm magnetic random-access memory based on perpendicular shape anisotropy, *Nanoscale* **10**, 12187 (2018).
- [53] O. Idigoras, A. K. Suszka, P. Vavassori, B. Obry, B. Hillebrands, P. Landeros, and A. Berger, Magnetization reversal of in-plane uniaxial Co films and its dependence on epitaxial alignment, *J. Appl. Phys.* **115**, 083912 (2014).
- [54] O. Idigoras, U. Palomares, A. K. Suszka, L. Fallarino, and A. Berger, Magnetic properties of room temperature grown epitaxial  $\text{Co}_{1-x}\text{Ru}_x$ -alloy films, *Appl. Phys. Lett.* **103**, 102410 (2013).
- [55] The base layer is fabricated with an additional 5% concentration of Pt to enhance its uniaxial anisotropy and, therefore, enhance the overall coercivity of the film. This enhancement, in turn, allows us to disentangle the reversal of the bottom and top FM layers more easily.
- [56] L. Fallarino, B. J. Kirby, M. Pancaldi, P. Riego, A. L. Balk, C. W. Miller, P. Vavassori, and A. Berger, Magnetic properties of epitaxial CoCr films with depth-dependent exchange-coupling profiles, *Phys. Rev. B* **95**, 134445 (2017).
- [57] P. Riego, L. Fallarino, C. Martínez-Olivier, and A. Berger, Magnetic anisotropy of uniaxial ferromagnets near the Curie temperature, *Phys. Rev. B* **102**, 174436 (2020).
- [58] X. Zhou, N. Vernier, G. Agnus, S. Eimer, W. Lin, and Y. Zhai, Highly Anisotropic Magnetic Domain Wall Behavior in In-Plane Magnetic Films, *Phys. Rev. Lett.* **125**, 237203 (2020).
- [59] B. J. Kirby, L. Fallarino, P. Riego, B. B. Maranville, C. W. Miller, and A. Berger, Nanoscale magnetic localization in exchange strength modulated ferromagnets, *Phys. Rev. B* **98**, 064404 (2018).
- [60] W. Yang, D. N. Lambeth, and D. E. Laughlin, Unicrystal Co-alloy media on Si (110), *J. Appl. Phys.* **85**, 4723 (1999).
- [61] A. Kirilyuk, J. Ferré, V. Grolier, J. P. Jamet, and D. Renard, Magnetization reversal in ultrathin ferromagnetic films with perpendicular anisotropy, *J. Magn. Magn. Mater.* **171**, 45 (1997).
- [62] R. W. Wang and D. L. Mills, Onset of long-range order in superlattices: mean-field theory, *Phys. Rev. B* **46**, 11681 (1992).
- [63] W. L. Lim, N. Ebrahim-Zadeh, J. C. Owens, H. G. E. Hentschel, and S. Urazhdin, Temperature-dependent proximity magnetism in Pt, *Appl. Phys. Lett.* **102**, 162404 (2013).

- [64] M. Gottwald, J. J. Kan, K. Lee, S. H. Kang, and E. E. Fullerton, Paramagnetic  $\text{Fe}_x\text{Ta}_{1-x}$  alloys for engineering of perpendicularly magnetized tunnel junctions, *APL Mater.* **1**, 022102 (2013).
- [65] G. Woltersdorf, M. Kiessling, G. Meyer, J.-U. Thiele, and C. H. Back, Damping by Slow Relaxing Rare Earth Impurities in  $\text{Ni}_{80}\text{Fe}_{20}$ , *Phys. Rev. Lett.* **102**, 257602 (2009).
- [66] S. Azzawi, A. Ganguly, M. Tokaç, R. M. Rowan-Robinson, J. Sinha, A. T. Hindmarch, A. Barman, and D. Atkinson, Evolution of damping in ferromagnetic/nonmagnetic thin film bilayers as a function of nonmagnetic layer thickness, *Phys. Rev. B* **93**, 054402 (2016).
- [67] R. A. Gallardo, P. Alvarado-Seguel, F. Brevis, A. Roldán-Molina, K. Lenz, J. Lindner, and P. Landeros, Spin-wave channeling in magnetization-graded nanostrips, *Nanomaterials* **12**, 2785 (2022).
- [68] S. Rao, S. Couet, S. Van Beek, S. Kundu, S. H. Sharifi, N. Jossart, and G. S. Kar, A systematic assessment of W-doped CoFeB single free layers for low power STT-MRAM applications, *Electronics* **10**, 2384 (2021).